Contrib Mineral Petrol (2002) 142: 397–415
DOI 10.1007/s004100100300

Susumu Ikeda · Mitsuhiro Toriumi · Hideto Yoshida
Ichiko Shimizu

Experimental study of the textural development of igneous rocks in the late stage of crystallization: the importance of interfacial energies under non-equilibrium conditions

Received: 5 October 2000 / Accepted: 23 July 2001 / Published online: 8 September 2001

Abstract Textural development of igneous rocks in the late stage of crystallization was experimentally studied using the diopside–anorthite and diopside-forsterite-anorthite systems. Isothermal, cooling, and heating experiments were performed within the temperature range in which the melt fraction was low (less than 25 vol%). Dihedral angles at solid-melt-solid triple junctions were measured as the indicator of the interfacial energy ratio (solid-melt interfacial energy/solid-solid grain boundary energy). In isothermal experiments, the dihedral angle (i.e. interfacial energy ratio) was large at low temperatures and small at high temperatures. The dihedral angle increased during cooling and decreased during heating compared to the equilibrium value. In cooling, crystal clustering and melt segregation were observed when the dihedral angle increased. The observed clustering threshold (dihedral angle$\sim$58°) in cooling experiments almost corresponded to the theoretical threshold (60°) which causes crystal clustering and melt segregation to minimize total interfacial energy under equilibrium conditions. These experimental results suggest that the change of dihedral angle under non-equilibrium conditions is a substantial phenomenon depending on the actual change of the interfacial energy ratio. Many kinds of clustering textures are observed in natural igneous rocks. Glomeroporphyritic texture in volcanic rock and clustering texture in granite were observed as examples of clustering textures in natural igneous rocks. Owing to the analogy between the natural clustering textures and experimental textures, a textural diversification process depending on interfacial energies is suggested.

S. Ikeda (✉) · M. Toriumi
Department of Complexity Science and Engineering,
Graduate School of Frontier Sciences,
University of Tokyo, Hongo, Bunkyo-ku,
Tokyo 113–0033, Japan
E-mail: ikeda@chem.s.u-tokyo.ac.jp

H. Yoshida · I. Shimizu
Department of Earth and Planetary Science,
Graduate School of Science, University of Tokyo,
Hongo, Bunkyo-ku, Tokyo 113-0033, Japan

Editorial handling: T.L. Grove

Introduction

Textural development of igneous rocks is a important phenomenon in the earth sciences. Rock texture contains much information about magmatic processes and, in particular, cooling process of magma (e.g. Kirkpatrick 1975, 1981; Lofgren 1980; Cashman 1990). Many experimental studies have been carried out to elucidate the textural development process (Lofgren 1974, 1983; Lofgren et al. 1979; Kirkpatrick 1974; Kirkpatrick et al. 1976, 1979; Donaldson 1976, 1979; Fenn 1977; Swanson 1977; Swanson and Fenn 1986; Naney and Swanson 1980; Muncill and Lasaga 1987, 1988; Tsuchiyama 1983, 1985). These experimental efforts focused on the early stage of crystallization process, namely, on crystal growth in the stage with high melt fractions. A few experimental studies investigated the relationship between the grain size of the groundmass and the cooling rate in the late stage of magma crystallization (e.g. Walker et al. 1976, 1978; Grove and Walker 1977). However, few experimental studies were carried out to address, for example, the change in spatial distribution of crystals and melt through the late stage to complete crystallization.

This late stage of crystallization with low melt fractions, as well as nucleation and growth in the early stage of crystallization, is considered to be a significant process determining the final texture of rocks. In the late stage, crystals necessarily contact each other owing to the high solid fraction. As emphasized by Hunter (1987), the effect of interfacial energies (i.e. textural equilibrium) will be significant in textural development subsequent to the beginning of crystal contact. Interfacial energies subsequent to crystal contact probably influence the final texture of the crystalline aggregate by influencing such features as the spatial distribution of crystals and

melt, although interfacial energies are also significant prior to crystal contact to give the characteristic aspect ratios of crystal shape. Hunter (1987) suggested the importance of the textural equilibrium on textural development in the late stage of crystallization and, in particular, in the formation of adcumulate texture in layered intrusions as an example. Bryon et al. (1994, 1995, 1996) studied the textural development of granitic rocks from the early to late stage of crystallization in three dimensions by serial sectioning natural specimens. However, the details of the textural development in the late stage of crystallization have not been revealed by experiments.

The present study deals with the late stage of crystallization with the starting materials of low melt fractions (less than 25 vol%). The binary system diopside (Di; $CaMgSi_2O_6$)–anorthite (An; $CaAl_2Si_2O_8$) (Osborn 1942) and the ternary system diopside (Di; $CaMgSi_2O_6$)–forsterite (Fo; Mg_2SiO_4)–anorthite (An; $CaAl_2Si_2O_8$) (Osborn and Tait 1952), both of which are very familiar to petrologists as simple basaltic systems, were used in the experiments. The cooling experiments were performed from the temperature at which many crystals already exist. One of the most significant discoveries in the present study was an increase in dihedral angle (interfacial energy ratio) during cooling. This increase inthe interfacial energy ratio causes crystal clustering and melt segregation. We discuss the textural diversification of igneous rocks from the viewpoint of such crystal clustering. Decrease in the dihedral angle during heating was also found in the present study and will be discussed in regards to crustal anatexis leading to formation of migmatite.

Theories of interfacial energies and melt behavior

It is well-known that the ratio of solid-liquid interfacial energy to solid-solid grain boundary energy (γ_{sl}/γ_{ss}) controls the equilibrium morphology, distribution, and connectivity of liquid (e.g. Smith 1948; Beere 1975; Bulau et al. 1979; von Bargen and Waff 1986; Laporte et al. 1997; Laporte and Provost 2000). The dihedral angle (θ) at a solid-liquid-solid triple junction is a measurable indicator of the interfacial energy ratio (γ_{sl}/γ_{ss}) and is generally used to discuss the morphology and connectivity of liquid (Fig. 1). The interfacial energy ratio (γ_{sl}/γ_{ss}) has a following simple relationship with the dihedral angle (θ):

$$\frac{\gamma_{sl}}{\gamma_{ss}} = \frac{1}{2\cos\frac{\theta}{2}} \quad (1)$$

when the solid phase is monomineralic and isotropic. The effects of crystal anisotropy were discussed by Waff and Faul (1992), Laporte and Watson (1995) and Faul (2000). Melt geometry and network in multiphase partially molten systems were also studied (e.g. Toramaru and Fujii 1986; Nakano and Fujii 1989). The systems previously studied experimentally in earth sciences can be divided into two categories: those that involve partially molten systems (e.g. Waff and Bulau 1979; Jurewicz and Watson 1984, 1985; Fujii et al. 1986; Toramaru and Fujii 1986; von Bargen and Waff 1988; Laporte 1994; Laporte and Watson 1995; Lupulescu and Watson 1999; Gaetani and Grove 1999) and those that are solid-aqueous fluid systems (e.g. Watson et al. 1990; Holness 1993, 1995; Watson and Lupulescu 1993; Mibe et al. 1998, 1999). Most of these dihedral angles were measured in regards to the connectivity of liquid in the crust and mantle. Many studies also deal with the influence of interfacial energies and melt geometry on the rheology of rocks (e.g. Cooper and Kohlstedt 1986).

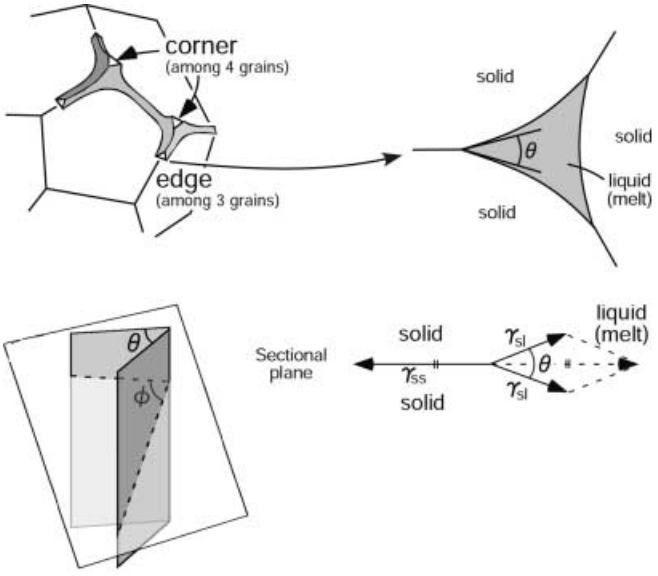

Fig. 1 Liquid (melt) geometry and dihedral angle (θ). Liquid exists in corners and along the edges in three dimensions. Dihedral angle is formed by the balance of interfacial energies (tensions) γ_{sl} and γ_{ss}. Observed (apparent) dihedral angle in the two-dimensional section (ϕ) changes with the cutting direction

Interfacial energies control not only liquid connectivity but also liquid infiltration and expulsion (e.g. Watson 1999). In the present study, the roles of the interfacial energies are emphasized. In materials sciences, Beere (1975) theoretically studied the relationship among volume fraction of melt, dihedral angle, and total interfacial energy with a three-dimensional model. In earth sciences, Watson (1982) studied the theoretical relationship between dihedral angle and total interfacial energy (Fig. 2a, left). The calculated results of these two studies suggested that liquid infiltrates the crystalline aggregate when $\theta < 60°$ and is expelled from aggregate when $\theta > 60°$ (Fig. 2a, right). Later, Park and Yoon (1985; with a 3-D model), Jurewicz and Watson (1985; with a 2-D model) and Laporte and Watson (1995; with bcc and fcc 3-D models) reached very interesting calculated results. The common conclusion of these three studies was that an equilibrium melt fraction exists which minimizes the total interfacial energy even with low dihedral angle less than 60° (Fig. 2b, left). Watson (1999) termed this melt fraction the ''minimum-energy

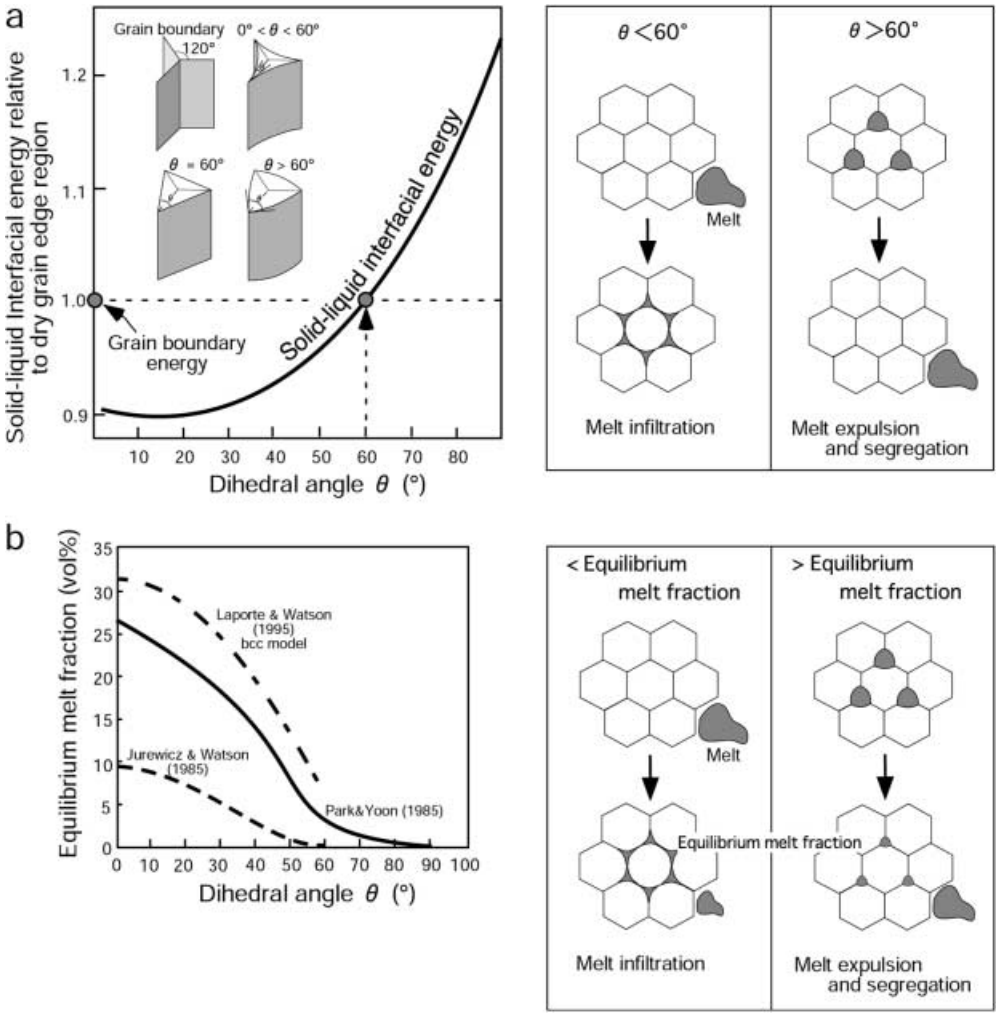

Fig. 2 **a** Relationship between dihedral angle and total interfacial energy (modified from Watson 1982). According to this diagram, melt infiltration into the crystal aggregate ($\theta < 60°$) and expulsion from the aggregate ($\theta > 60°$) will occur as shown on the *right*. **b** Equilibrium melt fraction versus dihedral angle (minimum energy melt fraction). Data from Park and Yoon (1985), Jurewicz and Watson (1985), and Laporte and Watson (1995). Schematic diagrams on the *right* indicate that the melt infiltration and expulsion occur when the melt quantity in the aggregate is different from the equilibrium melt fraction

melt fraction (MEMF)". If the concept of equilibrium melt fraction is correct, the melt infiltration and expulsion can occur due to the dihedral angle. If the melt fraction in the crystalline aggregate is less than the equilibrium melt fraction, additional melt can infiltrate the aggregate up to the equilibrium melt fraction. In contrast, when the crystalline aggregate includes melt exceeding the equilibrium melt fraction, the excess melt will be expelled from the aggregate (Fig. 2b, right).

These predictions of liquid behavior based on the interfacial energies have been confirmed by experiments. Melt infiltration under small dihedral angle condition was experimentally confirmed by Watson (1982). Riley Jr. and Kohlstedt (1991) also showed the melt infiltration under conditions of small dihedral angle by experiments with melt migration couples composed of olivine aggregate and silicate melt. Jurewicz and Watson (1985) experimentally demonstrated melt segregation under large dihedral angle conditions. They maintained the starting material of granitic composition isothermally (1,000 °C) under 10 kbar and obtained a texture consisting of clustered crystals and melt pools. The crystal clusters were considered to form by melt expulsion from the crystalline aggregate. Expelled melt gathered and formed melt pools to minimize total interfacial energy. Hunter (1987) applied this concept to the textural development of adcumulate formed in natural igneous intrusions. He mentioned the importance of the interfacial energies in the textural development of igneous rocks in the late stage of crystallization of magma.

Experiments

Starting materials

The starting materials in the diopside (Di)–anorthite (An) system (Fig. 3a) and in the diopside–forsterite (Fo)–anorthite system (Fig. 3b) were prepared with chemical reagents (SiO_2, Al_2O_3, MgO and $CaCO_3$). Chemical compositions of the materials were $Di_{90}An_{10}$ and $Di_{60}Fo_{30}An_{10}$ (wt% ratio), respectively. The mixtures of the reagents were completely melted and quenched. The quenched glass was ground to powder and annealed at the subsolidus temperature of 1,240 °C until crystallization was complete. Annealed $Di_{90}An_{10}$ consisted of diopside and anorthite crystals and $Di_{60}Fo_{30}An_{10}$ consisted of diopside, forsterite, and

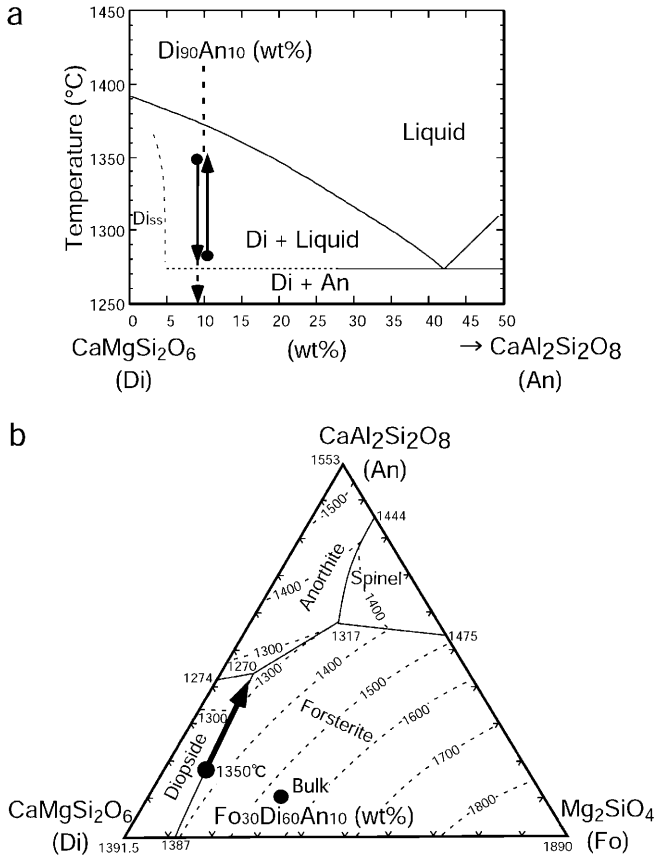

Fig. 3 **a** Phase diagram of the diopside-anorthite binary system (modified from Osborn 1942). Chemical composition of the starting material and experimental conditions (*arrows*) are also shown. **b** Phase diagram of forsterite-diopside-anorthite pseudo-ternary system (modified from Osborn and Tait 1952). Chemical bulk composition of the starting material and cooling pass (*arrow*) are also shown

anorthite crystals. They were ground to powder again and used in the experiments. The chemical compositions of the starting materials determined by X-ray fluorescence (XRF) are shown in Table 1 with ideal compositions for comparison.

Heating conditions

The starting material was put in the Pt-wire loop (4 mm in diameter) and heated in an ordinary electric furnace. Experiments were performed at room pressure because we could precisely control the cooling rate with the room pressure furnace. The Pt-wire loop has been widely used in many previous experimental studies in order to reduce the heterogeneous nucleation (e.g. Donaldson et al. 1975). The temperature calibration was performed using the melting points of Au (1,062.5° C) and diopside (1,391.5 °C). All heating conditions are listed in Table 2.

With $Di_{90}An_{10}$ starting material, isothermal cooling (0.5 and 0.05 °C/min) and heating experiments (0.5 °C/min) were performed. Isothermal experiments were carried out in order to investigate the equilibrium

Table 1 Ideal and XRF-analyzed chemical composition of the starting materials

	$Di_{90}An_{10}$		$Di_{60}Fo_{30}An_{10}$	
	Ideal	Analyzed	Ideal	Analyzed
SiO_2	54.27	54.4	50.43	49.5
Al_2O_3	3.66	3.7	3.66	3.7
MgO	16.75	16.6	28.36	29.6
CaO	25.32	24.6	17.55	18.0
Total	100.00	99.3	100.00	100.8

texture and the dihedral angle at each temperature. Cooling experiments were performed mainly from 1,350 °C. The specimen was held isothermally at 1,350 °C for 5 h before cooling in order to place the material near equilibrium at the temperature. When the specimen was held isothermally at 1,350 °C, rapid grain growth of diopside was observed during first two h, but the grain growth after 5 h was negligibly small. This is the main reason why the sample was held at 1,350 °C for 5 h before cooling. After the isothermal holding the specimen was cooled at 0.5 or 0.05 °C/min and quenched at each temperature (mainly above eutectic temperature). One sample was cooled to 1,150 °C (below eutectic temperature) for complete crystallization (run 14). Some samples were held at 1,280 °C (above eutectic temperature) after cooling from 1,350 to 1,280 °C (runs 15, 16). In the heating experiments, the specimen was held isothermally at 1,280 °C (above eutectic temperature) for 5 h and heated at 0.5 °C/min to each quenching temperature.

With $Di_{60}Fo_{30}An_{10}$ starting material, cooling experiments at 0.5 °C/min were mainly performed. The specimen was held isothermally at 1,350 °C for 5 h before cooling in order to place the material near equilibrium at the temperature. The isothermal holding condition (1,350 °C) was on the cotectic boundary curve where diopside, forsterite and melt coexist (Fig. 3b). After the isothermal treatment, the specimen was cooled at 0.5° C/min and quenched at each temperature.

Textural observation and chemical analyses of the run products

The textures of the run products were observed with the scanning electron microscope (SEM; JEOL JSM-840), primarily as back-scattered electron images. Bulk chemical compositions of the starting materials (Table 1) were determined by the XRF (PHILLIPS PW1480) system. The chemical compositions of the partial melt (quenched glass) were analyzed using the energy dispersive spectroscopy (EDS; Oxford Link ISIS) system attached to the SEM.

Determination of dihedral angle

The run products were investigated with respect to the chemical composition of the melt and the dihedral angles

Table 2 Run no. and heating conditions

With $Di_{90}An_{10}$ starting material	
[Isothermal experiments]	
Run 1	1,350 °C (retention 5 h)→quench
2	1,330 °C (retention 15 h)→quench
3	1,310 °C (retention 24 h)→quench
4	1,290 °C (retention 38 h)→quench
5	1,280 °C (retention 48 h)→quench
6	1,280 °C (retention 5 h)→quench
[Cooling experiments from 1,350 °C at 0.5 °C/min]	
8	1,350 °C (retention 5 h) – 0.5 °C/min→1,340 °C→quench
9	1,350 °C (retention 5 h) – 0.5 °C/min→1,330°C→quench
10	1,350 °C (retention 5 h) – 0.5 °C/min→1,320 °C→quench
11	1,350 °C (retention 5 h) – 0.5 °C/min→1,310 °C→quench
12	1,350 °C (retention 5 h) – 0.5 °C/min→1,290 °C→quench
13	1,350 °C (retention 5 h) – 0.5 °C/min→1,280 °C→quench
14	1,350 °C (retention 5 h) – 0.5 °C/min→1150 °C→quench
15	1,350 °C (retention 5 h) – 0.5 °C/min→1,280 °C (retention 9 h)→quench
16	1,350 °C (retention 5 h) – 0.5 °C/min→1,280 °C (retention 57 h)→quench
[Cooling experiments from 1,350 °C at 0.05 °C/min]	
18	1,350 °C (retention 5 h) – 0.05 °C/min→1,330 °C→quench
19	1,350 °C (retention 5 h) – 0.05 °C/min→1,310 °C→quench
20	1,350 °C (retention 5 h) – 0.05 °C/min→1,290 °C→quench
21	1,350 °C (retention 5 h) – 0.05 °C/min→1,280 °C→quench
[Heating experiments from 1,280 °C at 0.5 °C/min]	
22	1,280 °C (retention 5 h) – 0.5 °C/min→1,290 °C→quench
23	1,280 °C (retention 5 h) – 0.5 °C/min→1,310 °C→quench
24	1,280 °C (retention 5 h) – 0.5 °C/min→1,330 °C→quench
25	1,280 °C (retention 5 h) – 0.5 °C/min→1,350 °C→quench
With $Di_{60}Fo_{30}An_{10}$ starting material	
[Isothermal experiment]	
26	1,350 °C (retention 5 h)→quench
[Cooling experiments from 1,350 °C at 0.5 °C/min]	
27	1,350 °C (retention 5 h) – 0.5 °C/min→1,330 °C→quench
28	1,350 °C (retention 5 h) – 0.5 °C/min→1,310 °C→quench
29	1,350 °C (retention 5 h) – 0.5 °C/min→1,280 °C→quench
30	1,350 °C (retention 5 h) – 0.5 °C/min→1,100 °C→quench

at solid–melt–solid triple junctions. The dihedral angle appropriate to each specimen was determined by the method proposed by Riegger and Vlack (1960). The observed (apparent) dihedral angles (ϕ in Fig. 1) on two-dimensional sections of the three-dimensional specimen plot along a sigmoidal curve of the cumulative percent diagram if the specimen has a single true dihedral angle in three dimensions. The true dihedral angle in the specimen is close to the "median" of the observed dihedral angles. Taken strictly, the true dihedral angle is slightly different from the median. The difference (true angle minus median angle) is about $+1°$ when the true dihedral angle is between 30 and 60°. Error is estimated as about $\pm 4°$ (accuracy 96%, i.e. 2σ) when the true dihedral angle is between 30 and 60° and the number of observed points is around 100. In the present study, 100–200 dihedral angles were measured on each polished section and the true dihedral angle of the specimen was estimated by adding the correction value ($+1°$) to the median angle.

The determination of the dihedral angle is based on the assumption that a specimen has only one true dihedral angle. However, a specimen probably has many true dihedral angles because rock-forming minerals are anisotropic and have different interfacial energies for individual crystal faces. Therefore, each solid–melt–solid triple junction probably has a different dihedral angle. Jurewicz and Jurewicz (1986) calculated the apparent dihedral angle distributions for the case in which the true dihedral angle has a normal distribution. They showed that real distributions of natural rocks are similar to the calculated distribution whose true dihedral angle has a normal distribution with a standard deviation (1σ) up to 10°. In the present study, the distributions of observed (apparent) dihedral angles were also different from the theoretical distribution even in the specimen held isothermally (Fig. 4). These results suggest the wide distribution of the true dihedral angle even in a single sample. However, it is impossible to determine the true dihedral angles at each triple junction on the two-dimensional section. Thus, also in the present study, the median (strictly $+1°$) of the observed angles was used as a true dihedral angle appropriate to each specimen, according to the custom.

Observation of clustering textures in natural igneous rocks

We observed two types of clustering textures in natural igneous rocks. Glomeroporphyritic texture in volcanic

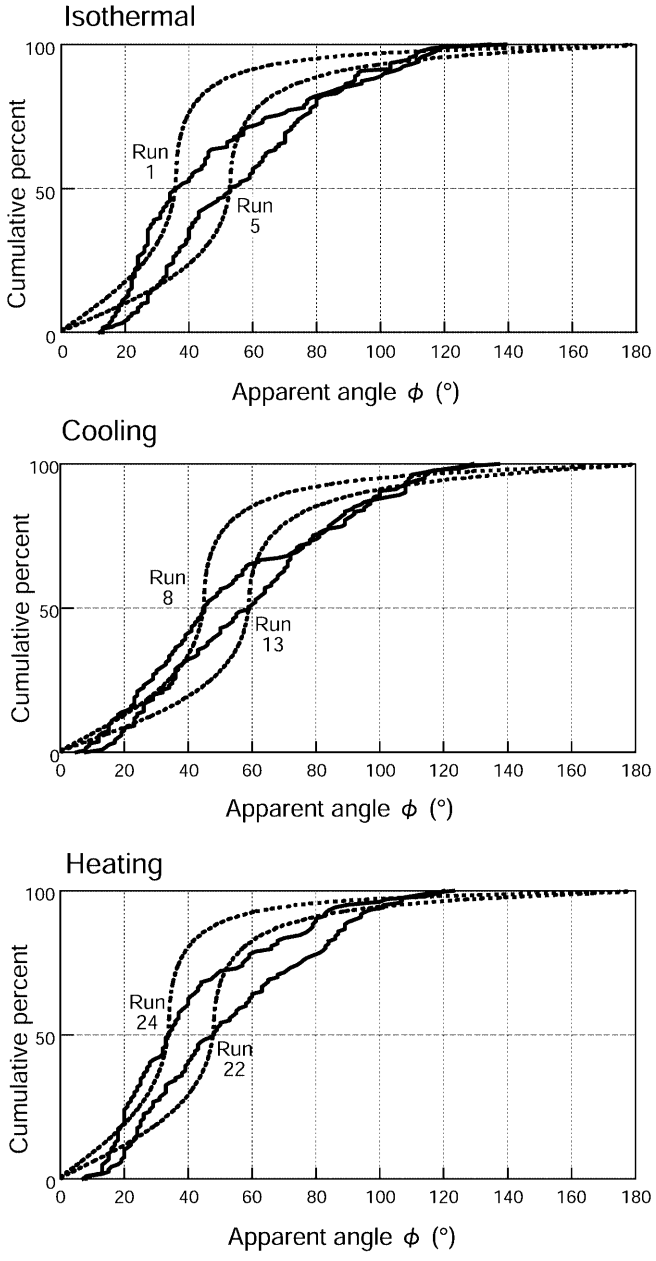

Fig. 4 Cumulative percent diagrams showing the distribution of observed (apparent) dihedral angles ϕ on two-dimensional sections. Two typical distributions of isothermal, cooling (0.5 °C/min) and heating (0.5 °C/min) experiments are shown. *Solid* and *dashed curves* indicate observed and theoretical distributions, respectively

rocks is obviously a clustering texture. Glomeroporphyritic texture with clear oscillatory zoning was used to elucidate the process of overgrowth and clustering. Many granites seem to have clustering texture of each constituent mineral. However, the feature of clustering in granites is not as obvious as the glomeroporphyritic texture. Thus, spatial distribution analysis was performed to judge the degree of clustering in natural granite specimens. The details of the observations follow.

Glomeroporphyritic texture

Glomeroporphyritic texture signifies clotting of crystal phenocrysts or a rock including such clots. Glomeroporphyritic texture is often observed in volcanic rocks, in particular, in diabase, andesite, and dacite (e.g. Williams et al. 1954; Bard 1986). We observed the glomeroporphyritic texture in an andesite from the Sakura-jima volcano. The most familiar type of clot in the specimen consisted of plagioclase phenocrysts (monomineralic). Each of the phenocrysts in the clots showed very clear zoning We used the zoning to investigate the crystal growth process, in particular, after contact of the phenocrysts. Two-dimensional element mapping was carried out with the wave length dispersive electron probe microanalyzer (JEOL JXA-8900L). Ca concentration was used to trace crystal growth because the concentration difference of Ca among zoning bands was the clearest in the measured elements.

Clustered texture in granite

We investigated two granite samples from Inada (Ibaraki Prefecture) and Hirukawa (Gifu Prefecture), Japan. Both of them are biotite-granite consisting of K-feldspar, plagioclase, quartz, and biotite. Potassium feldspar was stained (yellowish) with a Na-cobaltinitrite solution (e.g. Houghton 1980). After obtaining images of the stained plane, we made large thin sections ($\sim$ 5×4 cm^2) of the specimens (just the slices of those images) and identified all of the crystal grains (grain boundaries) in the thin sections by putting them between two polarizing plates. Binary images of each constituent mineral were made. The spatial distribution of each mineral was studied using these binary images as follows. First, the coordinates of the center of mass of the crystals were determined by image analysis with the software "Ultimage". In order to assess the degree of clustering, the "nearest neighbor spatial analysis method" proposed by Jerram et al. (1996) was used. The degree of order, randomness, and clustering is expressed by the index R.

$$R = \frac{r_A}{r_E}$$
$$r_A = \frac{\sum_{i=1}^{N} r_i}{N} \text{ and } r_E = \frac{1}{2\sqrt{\rho}} \quad (2)$$

where N is the number of particles, r_i is the distance to nearest neighbor i, and ρ is the number density of particles (N/area). In the case in which the volume fraction of the target mineral is zero (i.e. each grain is a dot having no volume), $R = 1$ indicates random distribution. In this case, $R > 1$ indicates ordered distribution and $R < 1$ clustered distribution. The actual R value in general cases in which crystals have finite volume (area in image) will be mentioned later.

Results

Dihedral angle measurements

The results of dihedral angle measurements are listed in Table 3 and plotted in Fig. 5. In Fig. 5, the variation of the dihedral angle is plotted in two forms. Figure 5a shows the relationship between the temperature and the dihedral angle. Figure 5b shows the relationship between the average chemical composition (Al_2O_3) of the partial melt and the dihedral angle.

The dihedral angles in the isothermal experiments are considered to be close to the equilibrium dihedral angles at each temperature. The dihedral angle was high at low temperatures. The dihedral angle was high with high Al_2O_3 (An component) concentration in melt. This tendency is consistent with the variation of the dihedral angle in many metallic binary systems, for example, Zn–Sn, Al–Sn, Zn–In, and Zn–Bi systems (e.g. Eustathopoulos et al. 1976; Passerone et al. 1977, 1979; Camel et al. 1980).

In the cooling experiments, increase in the dihedral angle was observed. The tendency of dihedral angle to increase with decreasing temperature and with increasing Al_2O_3 content in melt was the same as that of isothermal experiments. However, the dihedral angles in cooling experiments were always larger than those in the isothermal experiments when they were compared at the same temperature. The increase in the dihedral angle became larger with increasing cooling rate. The maximum difference between the non-equilibrium and equilibrium was 13° (at 1,310 °C), which corresponds to the increase in solid-melt interfacial energy about 6% according to Eq. (1) (on the assumption that the grain boundary energy does not depend on the temperature). The maximum dihedral angle was 61° at 1,280 °C in cooling experiment (0.5 °C/min). In silicate systems dihedral angles greater than 60° are very rare in equilibrium experiments (Harte et al. 1993; Laporte et al. 1997; Laporte and Provost 2000). It is also noteworthy that the maximum dihedral angle 61° at 1,280 °C in the cooling experiment dropped to 53 ° (equal to the equilibrium value at 1,280 °C) after cooling stopped and retention at 1,280 °C.

The dihedral angle was also measured in heating experiments from 1,280 °C (heating rate 0.5 °C/min). The dihedral angle at the start point of heating (after holding at 1,280 °C for 5 h) was 53°, which is almost the same as that of isothermal (equilibrium) experiment (1,280 °C, 48 h). Thus, the heating experiment was performed after isothermal holding for 5 h at 1,280 °C. The dihedral angles in heating experiments were always smaller than those in the isothermal experiments at the same temperatures.

Textural change in the experiments with $Di_{90}An_{10}$

The textural changes in the cooling experiments are shown in Fig. 6. Before cooling, the specimens were held at 1,350 °C for 5 h in order to allow the specimens to

Table 3 Data list of dihedral angle and Al_2O_3 concentration in the melt (starting material: $Di_{90}An_{10}$)

Run no.	Temp. (°C)	Retention time (h)	Dihedral angle (°)		Al_2O_3 (wt%) in melt	Error (1σ)
			(Median)	(Median + 1)		
[Isothermal]						
1	1,350	5	36	37	12.39	1.14
2	1,330	15	39	40	13.47	1.12
3	1,310	24	44	45	14.44	0.86
4	1,290	38	50	51	15.15	0.77
5	1,280	48	53	54	15.31	0.91
6	1,280	5	52	53	15.26	0.39
[Cooled from 1,350 °C at 0.5° C/min]						
8	to 1,340		45	46	12.69	0.59
9	to 1,330		51	52	12.90	0.89
10	to 1,320		54	55	13.51	0.46
11	to 1,310		57	58	14.04	0.98
12	to 1,290		57	58	14.71	0.45
13	to 1,280		60	61	14.89	0.84
15	to 1,280	9 h at 1,280 °C	52	53	15.21	0.27
16	to 1,280	57 h at 1,280 °C	52	53	15.44	0.54
[Cooled from 1,350 °C at 0.05 °C/min]						
18	to 1,330		45	46	13.39	0.59
19	to 1,310		50	51	14.30	0.66
20	to 1,290		53	54	15.03	0.53
21	to 1,280		54	55	15.28	0.50
[Heated from 1,280 °C at 0.5 °C/min]						
22	to 1,290		48	49	15.02	0.36
23	to 1,310		42	43	14.72	0.22
24	to 1,330		34	35	13.76	0.50
25	to 1,350		33	34	12.61	0.87

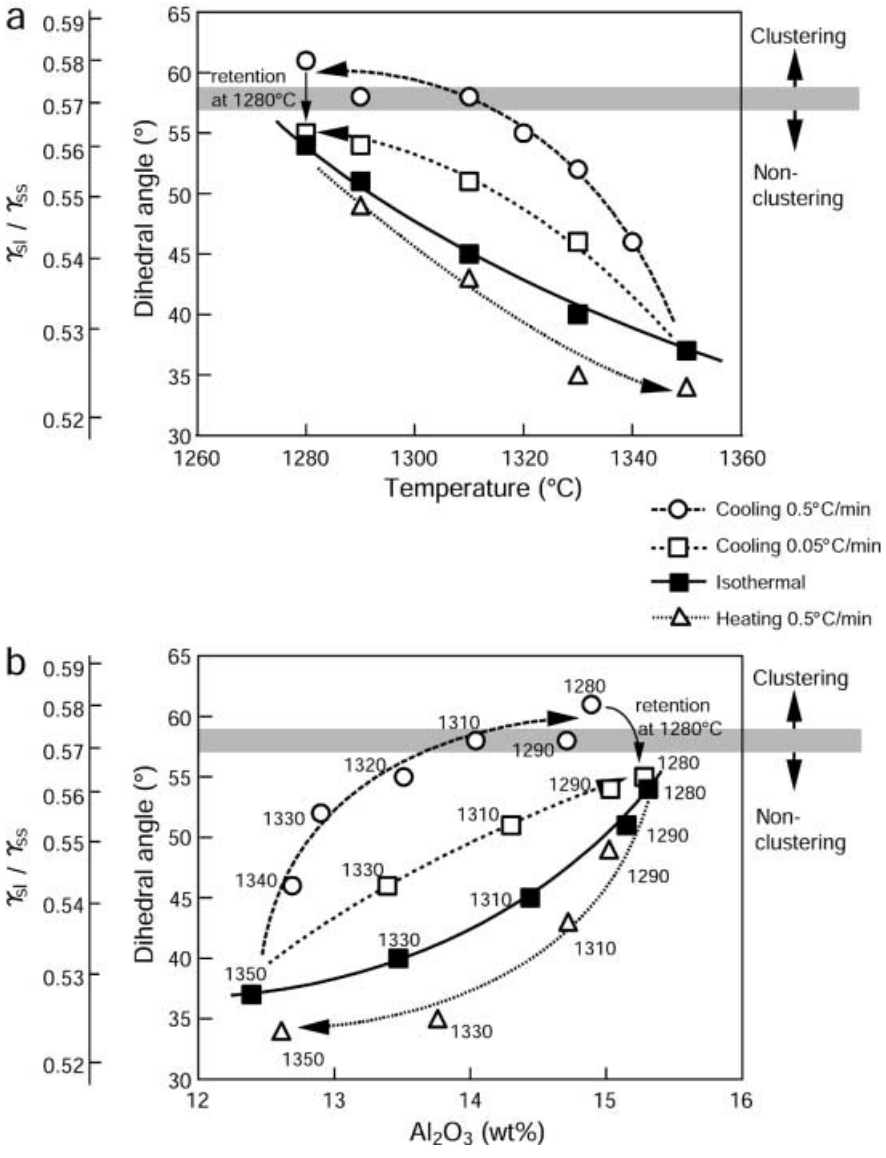

Fig. 5 **a** Variation of the dihedral angle with temperature. **b** Variation of the dihedral angle with Al_2O_3 concentration (anorthite component) in melt. *Error bars* were omitted to simplify the diagrams. *Error bars* of dihedral angle are considered to be around $\pm 4°$ (accuracy 96%, i.e. 2σ) according to the theory of Riegger and Vlack (1960). *Error bars* of Al_2O_3 concentration (1σ) are shown in Table 3. Numerical values near the points indicate run temperatures (in isothermal experiments) or quenched temperatures (in cooling and heating experiments)

approach equilibrium (Fig. 6a). The dihedral angle was 37° and most of the crystals were surrounded with the melt although they were partly connected with neighboring crystals. The specimen was then cooled at 0.5 or 0.05 °C/min. In the specimen cooled to 1,310 °C at 0.5 °C/min (run 11), the dihedral angle reached 58°, and clustering of diopside crystals and melt segregation are observable (Fig. 6b). In the specimen cooled to 1,280 °C (run 13, $\theta = 61°$), we observed clustering texture of diopside grains (Fig. 6c). Melt pockets within the clusters disappeared by overgrowth of surrounding crystals. The texture within a single diopside cluster is very similar to the adcumulus texture consisting of monomineralic aggregates without melt (Wager et al. 1960; Walker et al. 1988). This clustering texture is also similar to the plagioclase-chain structure discovered in natural basalt by Philpotts et al. (1998, 1999). Elsewhere in the specimen, the melt pools as shown in Fig. 6c were observed. The melt pools were very similar to those reported by Jurewicz and Watson (1985) with a granitic system.

We performed two additional types of experiment. One is that the specimen was cooled from 1,350 °C at 0.5 °C/min to 1,150 °C (run 14). In this experiment, the clustering texture of diopside crystals remained and

►

Fig. 6a–f Backscattered electron images of the specimens obtained in the cooling experiments (0.5 °C/min) with $Di_{90}An_{10}$ starting material. **a** Before cooling (after isothermal treatment at 1,350 °C for 5 h). **b** Cooled to 1,310 °C and quenched. Crystal clustering and melt segregation have started. **c** Cooled to 1,280 °C and then quenched. Crystal clustering and melt segregation were completed. **d** Cooling continued to 1,150 °C. Diopside clusters remained and anorthite crystallized fill the interstitial space among diopside clusters. **e** Cooling stopped at 1,280 °C, and then held at 1,280 °C for 9 h. Melt infiltration into the clusters (into grain boundaries) has started. **f** Cooling stopped at 1,280 °C, and then held at 1,280 °C for 57 h. The diopside clusters collapsed into individual diopside grains

anorthite crystallized between the diopside clusters (Fig. 6d). In the other experiment the specimen was cooled at 0.5 °C/min from 1,350 to 1,280 °C, and then held at 1,280 °C for 9 (run 15) or 57 h (run 16). The dihedral angle of 61° when the sample reached 1,280 °C decreased to 53° (the equilibrium value at 1,280 °C) in 9 h. Due to the decrease in the dihedral angle, the partial melt infiltrated the diopside clusters along the grain boundaries (Fig. 6e) and the clusters finally collapsed into individual crystal grains (Fig. 6f).

The textural change observed in the cooling experiments at 0.5 °C/min is summarized schematically in Fig. 7. Diopside crystals formed clusters with the increase in the dihedral angle during cooling. Clustering is caused by the melt expulsion from the crystalline aggregate. The clustering texture remained with continued cooling. On the other hand, the clustering texture collapsed into individual crystals by isothermal holding at 1,280 °C with a decrease in the dihedral angle to the equilibrium value. In the specimen cooled at 0.05 °C/

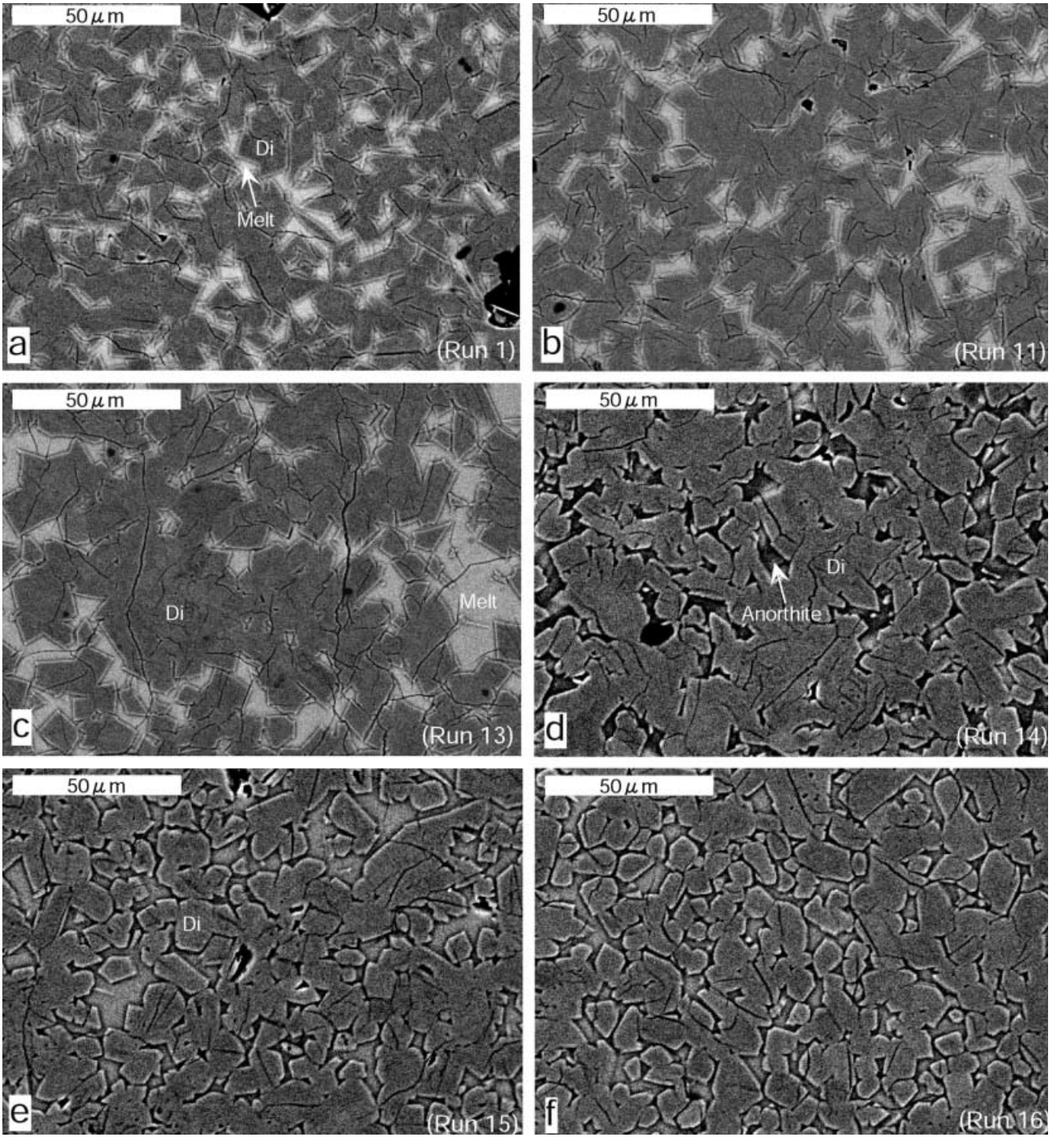

min, a similar but less well developed textural change (crystal clustering and melt segregation) was observed. In isothermal experiments between 1,350 and 1,280 °C, in which the dihedral angle ranged from 37° to 53°, such textural change was not observed.

Textural change in the experiments with $Di_{60}Fo_{30}An_{10}$

The starting material was held at 1,350 °C (5 h) on the cotectic boundary curve where diopside, forsterite and melt coexist (Fig. 8a). Following isothermal processing, the specimen was cooled at 0.5 °C/min. During cooling, the diopside crystals began to form clusters including forsterite grains (Fig. 8b). This suggests that the coexisting minor minerals are involved in the clustering of the major mineral grains. Melt-concentrated areas were also observed, in which the grain size of each crystal was large and the crystals formed larger clusters (Fig. 8c). The clustering texture remained with continued cooling and finally anorthite crystallized between the diopside-forsterite clusters (Fig. 8d).

Observation of clustering textures in natural igneous rocks

Glomeroporphyritic texture

Figure 9 shows the two-dimensional distribution of Ca concentration in the glomeroporphyritic texture consisting of plagioclase phenocrysts. Very clear zoning is observed in the plagioclase phenocrysts in the clot. The origin of the albite-rich core is not evident. Here, we only regarded the anorthite-rich rim showing the oscillatory zoning. (Various explanations exist for the origin of the albite-rich core, for example, magma mixing after formation of the core, but the correct interpretation is not clear Thus, we dealt with the crystal growth process recorded only in the oscillatory zoning of the rim part.) Since all of the phenocrysts have zoning bands with the same Ca concentrations, we could trace the crystal growth history. Figure 10 shows the crystal growth history based on the Ca concentration. In Fig. 10b phenocrysts are growing individually in melt without any obstacles. In Fig. 10c phenocrysts contact each other and crystal growth begins to be restricted. Although crystal growth to the outer side is free, growth to the inner side can progress only in the melt pocket surrounded by phenocrysts. Surprisingly, phenocrysts overgrow and fill the melt pocket surrounded by themselves from c to f. In Fig. 10f the melt pocket is almost completely filled by grown phenocrysts. The plagioclase component was clearly sequentially added to the melt pocket from somewhere during the overgrowth of the phenocrysts. If not, the residual liquid in melt pocket would be depleted in plagioclase component during the overgrowth of plagioclase phenocrysts. Thus, the ''melt pocket'' may possibly have been connected by channels to the surrounding melt in three dimensions.

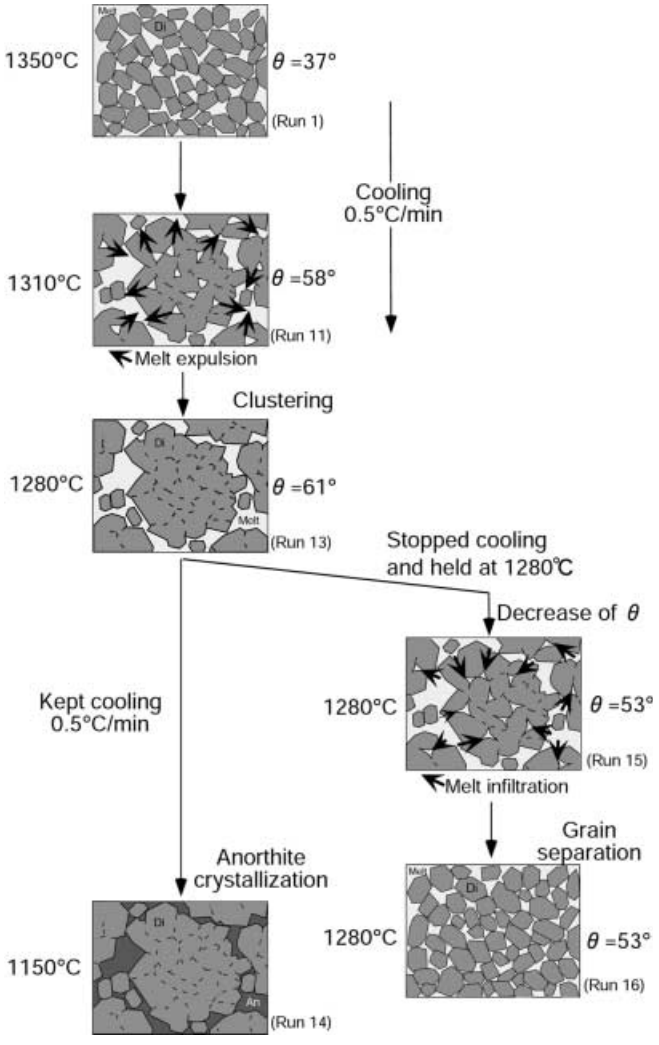

Fig. 7 Schematic diagrams of textural development observed in the cooling experiments (0.5 °C/min) using $Di_{90}An_{10}$ starting material

Clustered texture in granite

We investigated two granite specimens from Inada (Ibaraki Prefecture) and Hirukawa (Gifu Prefecture), Japan. Both are biotite-granite consisting of K-feldspar, plagioclase, quartz, and biotite. Figure 11 shows the entire image of the granite sample from Inada and the binary images of each constituent mineral. The results of the spatial distribution analysis using ''nearest neighbor spatial analysis method'' proposed by Jerram et al. (1996) are shown in Table 4. The results from the Hirukawa granite specimen are also show in Table 4. The degree of order, randomness, and clustering is expressed by the index *R*. When the volume fraction of the target mineral is zero (i.e. each grain is a volumeless point),

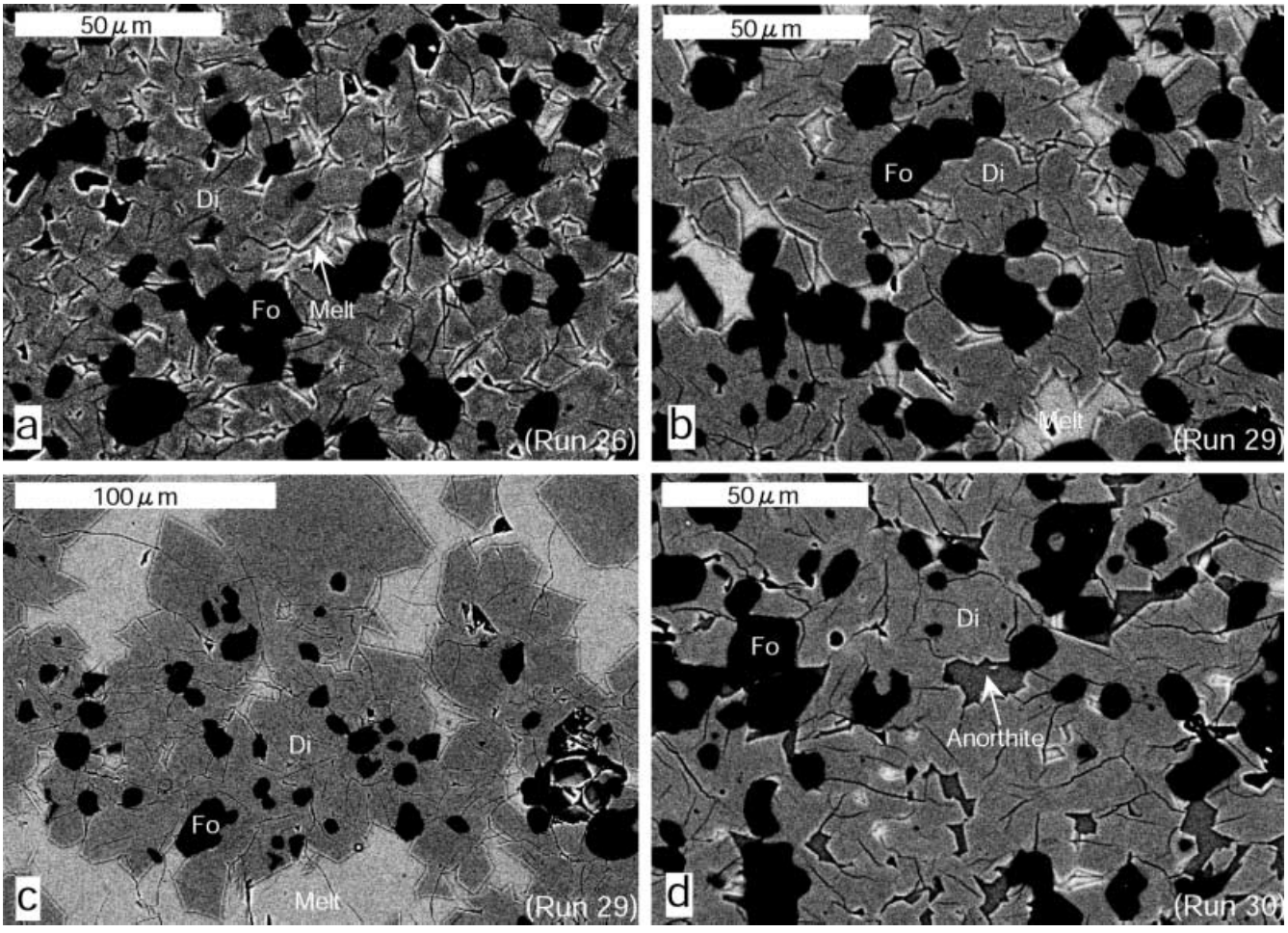

Fig. 8a–d Backscattered electron images of the specimens obtained in the cooling experiments (0.5 °C/min) in with $Di_{60}Fo_{30}An_{10}$ starting material. **a** Before cooling (after isothermal treatment at 1,350 °C for 5 h). **b, c** Cooled to 1,280 °C and quenched. **d** Cooling continued to 1,100 °C and then quenched. Anorthite crystallized

$R = 1$ indicates random distribution. $R > 1$ indicates ordered and $R < 1$ clustered distribution. The R value of random distribution is influenced and changed by the volume fraction of the target mineral. The R value of random distribution increases with increasing volume fraction (i.e. mode) of the target mineral (Fig. 12). Therefore, the level (R value) of random distribution needs correction with respect to the volume fraction of each target mineral.

The R values are in general less than the R of random distribution, except for biotite crystals in the Inada granite. Therefore, the spatial distribution of the crystals of each phase, at least of K-feldspar, plagioclase, and quartz, is considered to be clustered in those two granite specimens. Furthermore, each cluster rarely contains different crystalline phases. Each cluster is similar to the "adcumulate" which consists of phenocrysts of the monomineralic phase and contains no melt pocket (Wager et al. 1960). This is a significant aspect which corresponds to that observed in the glomeroporphyritic texture discussed above.

Discussion

Dihedral angle under equilibrium conditions

According to the results of isothermal experiments, the equilibrium dihedral angle seems to depend on the chemical composition of partial melt (Fig. 5b; solid curve). The dihedral angle at the diopside-melt-diopside triple junction tends to increase with increasing Al_2O_3 concentration (anorthite component) in the melt. Such a tendency has been observed in many metallic binary systems, for example, Cu–Pb, Zn–Sn, Al–Sn, Zn–In, and Zn–Bi systems (e.g. Eustathopoulos et al. 1974a, 1976; Passerone et al. 1977, 1979) and has been discussed theoretically in conjunction with thermodynamics and statistical mechanics (e.g. Eustathopoulos et al. 1974b; Takei and Shimizu 2001). The theoretical studies suggested that the solid–liquid interfacial energy depends on the chemical composition of the melt. The interfacial energy tends to increase with depletion of the solid component in the melt. The interfacial energy ratio (γ_{sl}/γ_{ss}) and the dihedral angle are thought to increase with depletion of the solid

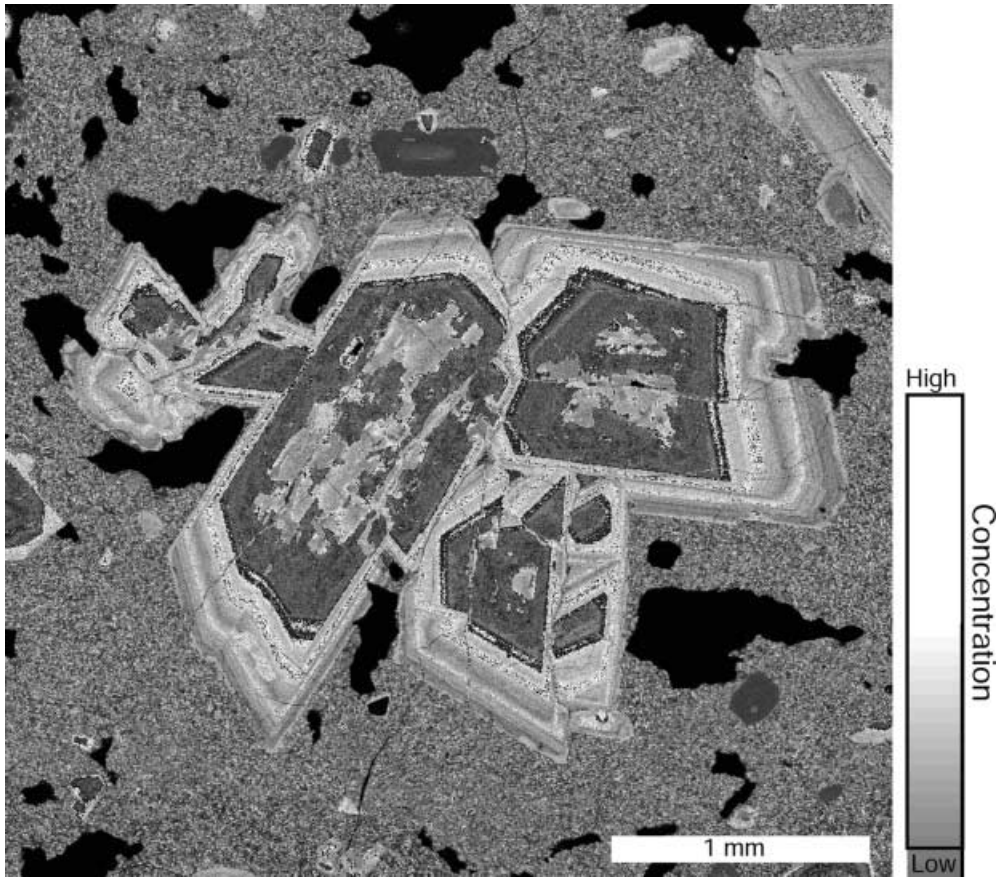

Fig. 9 Two-dimensional Ca concentration map of the glomeroporphyritic texture in andesite specimen from the Sakura-jima volcano

component in the melt. The following discussion of the non-equilibrium interfacial energies will be based on this compositional-dependence hypothesis.

Dihedral angle, interfacial energy and texture under non-equilibrium conditions

The difference of between the dihedral angle and the equilibrium values under the non-equilibrium conditions is one of the important results reached in the present study. The dihedral angles in cooling process were always greater than those in isothermal (equilibrium) experiments when they were compared at the same temperatures (Fig. 5). In contrast, the dihedral angles in the heating process were always smaller than those in isothermal experiments. Askay et al. (1974) suggested that the dihedral angle in a solid–liquid coexisting system decreases during the chemical reaction (non-equilibrium condition) because the free energy reduction during the early stage of the chemical reaction occurs only along the solid-liquid interface. The increase in the dihedral angle during cooling observed in this study cannot be explained by their theory.

Fortunately, the increase and decrease in the dihedral angle and textural change as well were observed during the present study. Comparison of the dihedral angle and texture allows discussion of whether the change of dihedral angle under non-equilibrium conditions is due to the change of interfacial energy ratio (γ_{sl}/γ_{ss}) or, if instead, change of the dihedral angle is not dependent on the interfacial energy ratio. In the cooling experiment at 0.5 °C/min, melt expulsion and crystal clustering began when the dihedral angle was greater than 58° (1,310 °C) and were completed when the dihedral angle reached 61° (1,280 °C). On the other hand, melt infiltration and cluster were observed when cooling of the specimen was stopped and the dihedral angle decreased to 53° (Fig. 6f). The boundary between clustering and non-clustering can be drawn at around $\theta \sim 58°$ in Fig. 5. This value is close to the theoretical threshold ($\theta = 60°$) between melt infiltration and melt expulsion based on the total interfacial energy under equilibrium conditions as shown in Fig. 2a. This suggests that the change of dihedral angle under non-equilibrium conditions does indeed depend on the change in the interfacial energy ratio.

We advance the hypothesis that the change in the dihedral angle under non-equilibrium conditions results from formation of a compositional boundary layer in the melt surrounding the crystals. Such boundary layers are know to form around crystals during dissolution or growth (e.g. Donaldson 1975; Lasaga 1998; Ikeda and Nakashima 1999). A compositional boundary layer was actually observed by line analysis using EDS in a specimen from a cooling experiment (Fig. 13d). As mentioned above, the solid–melt interfacial energy (dihedral angle)

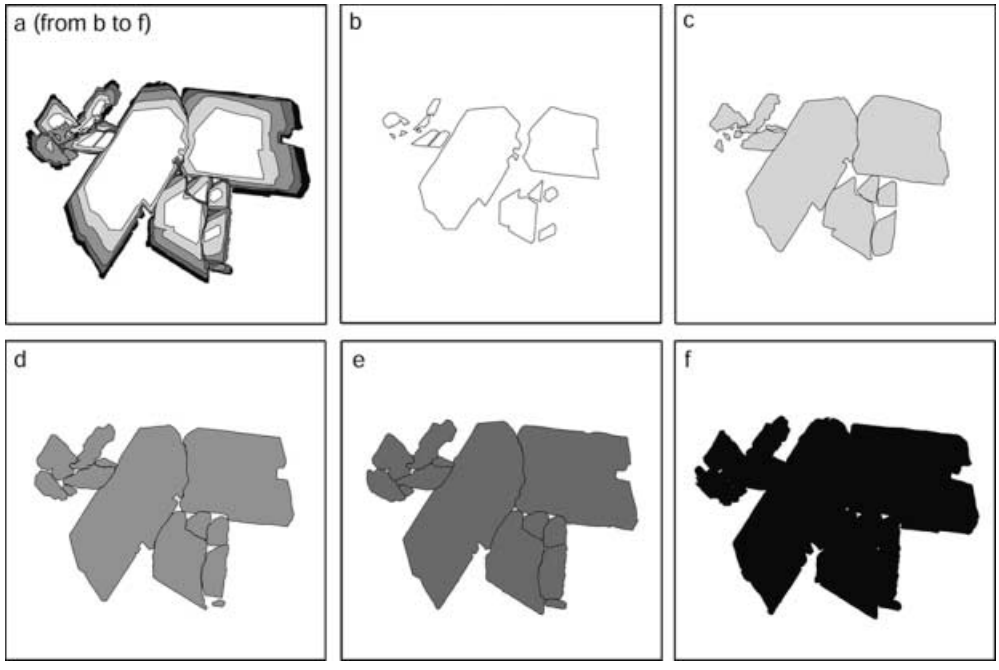

Fig. 10a–f Crystal growth process traced using the Ca concentration map shown in Fig. 9. The melt pockets surrounded by plagioclase phenocrysts are gradually filled due to the overgrowth of the phenocrysts

depends on the chemical composition of the melt under equilibrium conditions. It seems possible that the dihedral angle changes depending on the change of the chemical composition of the melt just touching the crystal surface under non-equilibrium conditions. During cooling (crystal growth), for example, the solid–melt interfacial energy (γ_{sl}) increases depending on the boundary layer rich in the anti-crystal components (Fig. 13b). Here, we assume that the solid–solid grain boundary energy (γ_{ss}) does not change in the narrow cooling temperature range. Since the small dihedral angle cannot satisfy Eq. (1), the dihedral angle was increased in order to satisfy the equation (Fig. 13c). This process requires significant material transport towards the groove (solid–melt–solid triple junction). According to this model, the response of the dihedral angle may be too late to some extent for the change of interfacial energy ratio. The fact that the experimental clustering threshold ($\theta \sim 58°$) is smaller than the theoretical threshold ($\theta = 60°$) may depend on a delayed response by the dihedral angle to the change in the interfacial energy ratio. Under an equilibrium condition, $\gamma_{sl}/\gamma_{ss} \cong 0.577$ when $\theta = 60°$ from Eq. (1). During the cooling experiment, γ_{sl}/γ_{ss} may have already exceeded 0.577 when $\theta = 58°$. However, this difference of 2° in the dihedral angle is also considered to be an error in measurement and may be of no significance.

The decrease in dihedral angle in the heating experiments can also be explained by the same concept. The boundary layer rich in the solid component is formed during a dissolution (melting) process and probably decreases the solid melt interfacial energy and the dihedral angle.

If this boundary layer model is correct, the change in the interfacial energy ratio will occur in many geological systems. However, too many kinetic parameters remain to be elucidated (e.g. diffusion coefficients of components in the melt, along the crystal-melt interface, and along the grain boundary) to confirm the boundary layer model. As such, the boundary layer model is presented here merely as a hypothesis.

The equilibrium dihedral angles in the magmatic systems are generally low ($\theta < 60°$) (Harte et al. 1993; Laporte et al. 1997; Laporte and Provost 2000) and crystal clustering did not seem likely to occur in natural igneous bodies. However, our new experimental results may modify this contention. If the crystals have the opportunity to come into contact, and if the interfacial energy ratio increases and exceeds the clustering threshold ($\gamma_{sl}/\gamma_{ss} \sim 0.577$; $\theta \sim 60°$) due to cooling effects, the crystal clustering may also occur in natural magmatic systems.

Natural rock texture and a textural diversification model

Various types of clustering textures exist in natural igneous rocks as mentioned above. A glomeroporphyritic texture is often observed in volcanic rocks, particularly in diabase, andesite, and dacite (e.g. Williams et al. 1954; Bard 1986). The most familiar type is the plagioclase phenocryst clots. Clots of pyroxene and clots consisting of both plagioclase and pyroxene are also observed. A glomeroporphyritic texture generally has a high melt fraction (large quantity of groundmass around the clots) and does not match the title of this paper. However, the mechanism involved in the formation of this texture is considered to be related to the experimental results of

the present study and its textural development is discussed here.

According to the result of Fig. 10, glomeroporphyritic texture was formed by filling the melt pocket following phenocrysts contact. In natural systems, except for the monomineralic rock systems such as anorthosite, the melt (pocket) surrounded by the plagioclase phenocrysts would deplete the plagioclase components during the overgrowth of the phenocrysts and growth would be restricted. However, plagioclase phenocrysts actually overgrew and filled the melt pocket. Such a growth mechanism is similar to the schematic illustration of adcumulate formation proposed by Hunter (1987). If the solid–melt interfacial energy is high enough to expel the melt from the phenocryst aggregate, formation of the a glomeroporphyritic texture is possible. The glomeroporphyritic texture is thought to form if the phenocrysts have the opportunity to come into contact with each other and if the interfacial energy ratio increases due to the cooling effects discussed in the present study. It is also possible that the glomeroporphyritic texture collapses into individual crystals owing to melt infiltration as shown in Fig. 6f if the interfacial energy ratio (dihedral angle) decreases for various reasons.

Clustering textures can be seen even in granitic rocks. (Of course, we do not assert that all granitic rocks have such clustering texture.) The degree of order, randomness, and clustering is expressed by the index R (Table 4). The R values are generally less than the R of random distribution, except for biotite crystals in the Inada granite. Therefore, the spatial distribution of the crystals of each mineral phase is considered to be clustered in

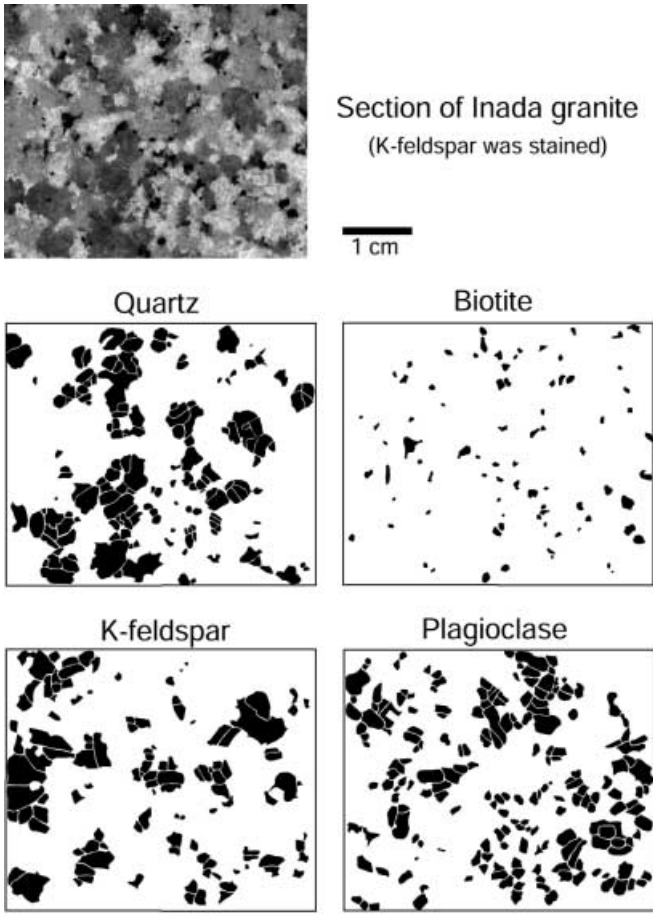

Fig. 11 Spatial distribution of crystals of each mineral in the Inada granite. The polished section of the specimen was stained (*upper image*) and made into a thin section. All crystal grains (grain boundaries) were identified in the thin sections by putting them between two polarizing plates. *Lower* Four images show the binary images of each constituent mineral, quartz, biotite, K-feldspar, and plagioclase

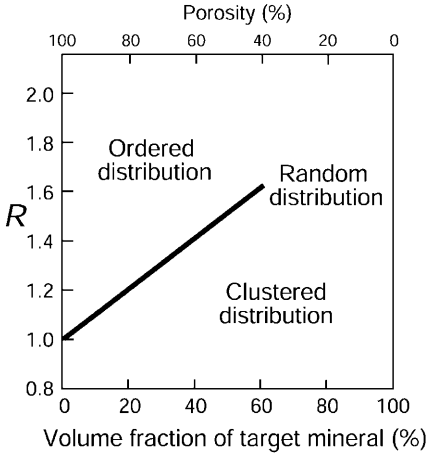

Fig. 12 R value of random distribution in the "nearest neighbor spatial analysis method" judging the spatial distribution of crystals. *Solid line* indicates the random distribution, i.e. the boundary between ordered and clustered distributions (modified from Jerram et al. 1996). In the original paper by Jerram et al., the boundary line was described versus porosity excepting target material (1 phase) as shown above this diagram

Table 4 Spatial distribution of crystals by the nearest neighbor spatial analysis method

	Mineral	R value	Mode	R of random distribution (from Fig. 12)	Distribution
Inada granite	Quartz	0.91	30	1.35	Clustered
	Biotite	1.04	5	1.10	~Random
	K-feldspar	0.91	24	1.30	Clustered
	Plagioclase	1.02	41	1.45	Clustered
Hirukawa granite	Quartz	1.04	30	1.35	Clustered
	Biotite	0.90	2	1.05	Clustered
	K-feldspar	1.25	39	1.40	Clustered
	Plagioclase	1.12	30	1.35	Clustered

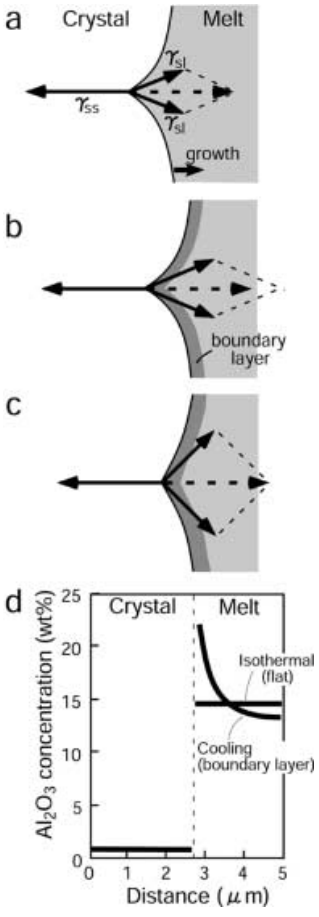

Fig. 13a–d Schematic illustrations of the hypothesis explaining the increase in the dihedral angle during cooling. **a** Equilibrium state satisfying Eq. (1). **b** Al-rich boundary layer is formed around diopside crystals during cooling (crystal growth). Solid-melt interfacial energy increases depending on the chemical composition (Al-rich) of melt just touching the crystal surface. If the dihedral angle is maintained, such a state does not satisfy Eq. (1). **c** Dihedral angle increases to satisfy Eq. (1). **d** Results of line analysis of Al_2O_3 concentration by the SEM-EDS (*isothermal*: run 3; *cooling*: run 11; both at 1,310 °C). These line profiles were modified on the assumption that the X-ray emission by 1 μmϕ electron probe has spatial distribution expressed by Gaussian function with full-width at half-maximum of 1.5 μm. Raw profiles were broader owing to the wide X-ray emission area

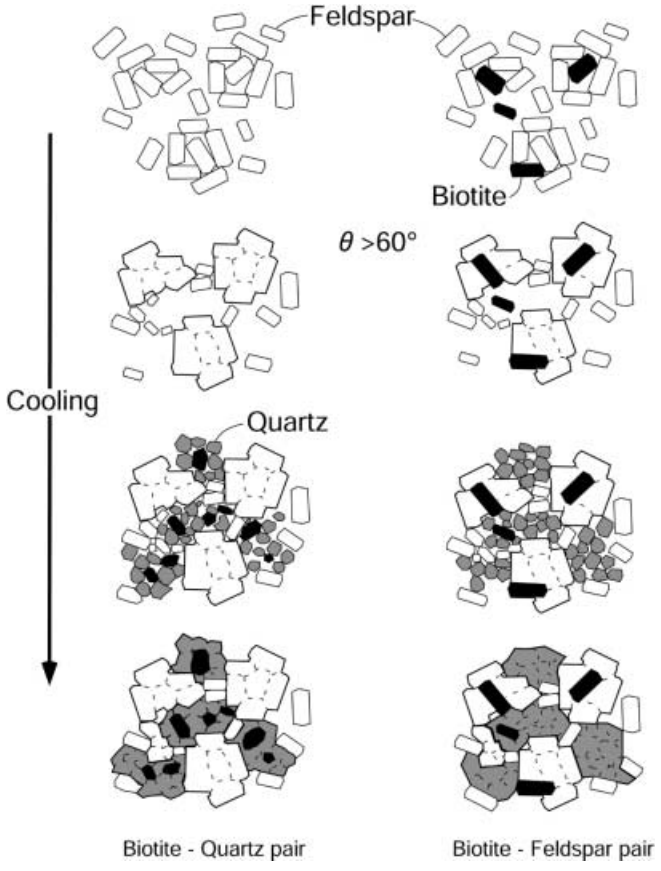

Fig. 14 Models of textural development of granitic textures during cooling. The models to the *left* and *right* differ in the crystallization sequence with respect to biotite. Such difference occurs, for example, due to the H_2O content in the system (Maaløe and Wyllie 1975)

those two granite specimens. Furthermore, each cluster rarely has different crystalline phases in it. The clusters of crystals are similar to the adcumulate which consists of phenocrysts of the monomineralic phase and has no melt pocket within it. This is a significant aspect which corresponds to that observed in the glomeroporphyritic texture discussed above.

The development of the clustered textures observed in granite specimens can be explained as shown in Fig. 14. This diagram shows two cases of textural development dependent on variation of the sequence of crystallization with respect to biotite. It is assumed that feldspar is the first mineral to crystallize from the melt (K-feldspar and plagioclase are not distinguished here). The crystallization sequence of biotite depends largely on the H_2O content of the system (Maaløe and Wyllie 1975). The model on the left shows a sequence in which biotite crystallizes primarily with quartz (low H_2O conditions). The model to the right shows a sequence in which the biotite crystallizes primarily with feldspar (high H_2O conditions). In the model to the left, feldspar crystals crystallize first crystallizing from the melt. If the solid–melt interfacial energy increases and exceeds the clustering threshold ($\gamma_{sl}/\gamma_{ss}\sim0.577$; $\theta\sim60°$), contacted feldspar crystals begin to form adcumulate-like clusters by expulsion of melt. As a result of the clustering of feldspar, the area is limited in which subsequent minerals (quartz and biotite) crystallize. Thus, quartz and biotite crystallize in the space between the feldspar clusters. The spatial distribution of quartz crystals necessarily becomes clustered. Furthermore, if the quartz-melt interfacial energy (qtz–melt–qtz dihedral angle) increases and the exceeds the clustering threshold, quartz crystals begin forming adcumulate-like clusters by expulsion of the melt. At the same time, the biotite crystals will be included in quartz clusters as shown in the Di–Fo–An system experiment (formation of diopside clusters including some forsterite crystals; Fig. 8b, c). On the other hand, in the right model, feldspar and biotite crystals co-crystallizes early from the melt. If the solid–melt interfacial energy increases and exceeds the

clustering threshold, contacted feldspar crystals begin to form adcumulate-like clusters by expulsion of melt. Biotite crystals are included in the feldspar clusters. After the feldspar-biotite clusters form, the space for quartz crystallization is limited, and the spatial distribution of quartz crystals necessarily becomes clustered. Furthermore, if the quartz-melt interfacial energy (qtz–melt–qtz dihedral angle) increases and the exceeds the clustering threshold, quartz crystals begin forming adcumulate-like clusters by expulsion of the included melt.

Actually, both types of clustering texture can be observed in natural granitic rocks. For example, Morishita and Obata (1995) reported the close spatial association between biotite and quartz in their granitic specimen. The close spatial association presumably indicates that biotite grains are mainly included in quartz clusters. Granitic rocks with the feldspar-biotite pair are also observed in nature.

The observed equilibrium dihedral angles of granitic systems have wide range from 10 to 60° (e.g. Laporte et al. 1997). If the equilibrium dihedral angle is large, only little cooling effects (increase in solid–melt interfacial energy) are required for crystal clustering. However, the cooling effect is required for clustering when the equilibrium dihedral angle is small.

The discussion above allows proposal of a preliminary model to produce the textural variation found in igneous rocks. Four processes are shown in Fig. 15. Processes a and b are for plutonic rocks and *c* and d for volcanic rocks. In all of the processes, the dihedral angle (solid–melt interfacial energy) is considered to increase with decreasing temperature even under equilibrium conditions, because the chemical composition of the melt generally changes in the direction opposite to those of crystals with decreasing temperature. When the interfacial energy ratio exceeds the clustering threshold ($\gamma_{sl}/\gamma_{ss}\sim0.577$; $\theta\sim60°$), the melt pockets surrounded by the crystals are probably expelled and adcumulate-like clustering texture will be formed (Fig. 15a, c). In such a case, the final spatial distribution of crystals does not correspond to the early distribution of nucleation. On the other hand, if there is no chance to exceed the clustering threshold, clustering does not occur. In this case, the final spatial distribution of crystals corresponds to the early distribution of nucleation if the crystals do not move by gravity. If the nucleation sites are random and accumulation does not occur, the final texture will have a random spatial distribution of crystals (Fig. 15b, d).

Of course, in the sequence of crystallization of actual igneous systems, the temperature ranges of the crystallization of minerals generally overlaps, thus, the degree of clustering will be lower than that in the above models. Crystal clusters will sometimes include other kinds of mineral grains as shown in Fig. 8c. For example, feldspar clusters and quartz clusters in natural granite sometimes include quartz and feldspar grains, respectively. A natural glomeroporphyritic texture of plagioclase phenocrysts often includes other kinds of mineral grains such as pyroxene.

Heating system

In this paper, we reported primarily the increase of the interfacial energy ratio (dihedral angle) during cooling which causes crystal clustering and melt segregation.

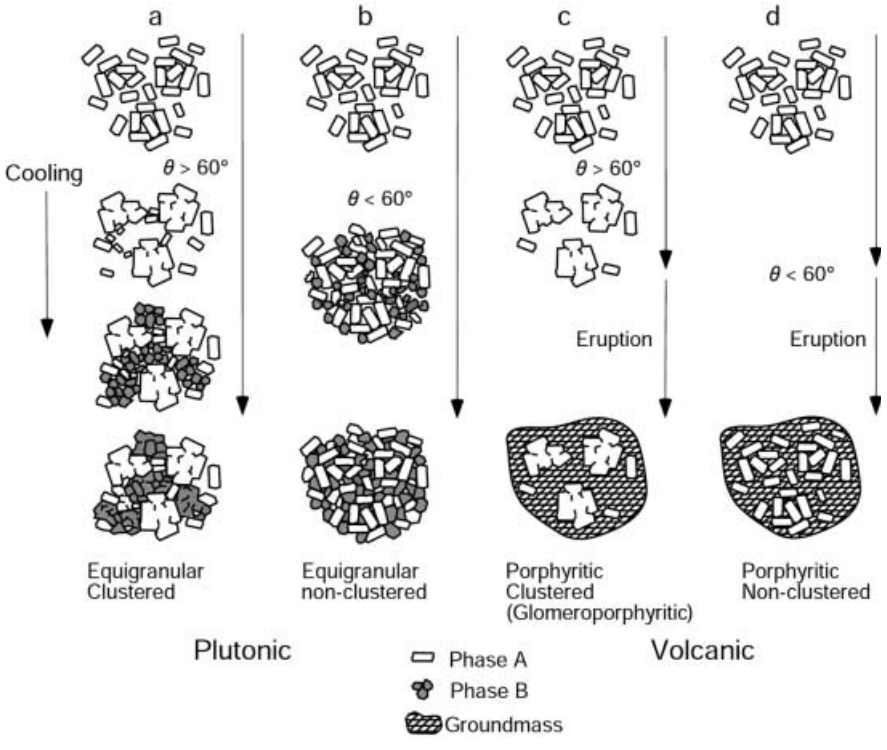

Fig. 15a–d Textural diversification model depending on the interfacial energy ratio (dihedral angle). The system with a large dihedral angle produces clustering texture in both plutonic and volcanic rocks. Of course, crystal contact is required for clustering in volcanic rocks whose melt fraction is generally high

However, the decrease in interfacial energy ratio during heating is also an important result. Partially melting regions are thought to exist in the earth's interior. For example, migmatite is considered to be formed by partial melting (anatexis) of crustal rocks. Watson (1999) suggested a melt segregation mechanism during migmatite formation which depends on the interfacial energy (minimum–energy melt fraction). A melt which exceeds the equilibrium melt fraction can segregate during migmatite formation. The results of our cooling and heating experiments give the concept of melt segregation an additional constraint. The crustal material is heated and melts partially in the early stage of anatexis. During the heating process, the solid–melt interfacial energy (dihedral angle) probably tends to decrease, such that melt segregation by expulsion is not likely to occur. On the contrary, the solid–melt interfacial energy tends to increase in the cooling process. Therefore, melt segregation is likely to occur in cooling process during migmatite formation.

Conclusions

In order to investigate the textural development in the late stage of crystallization, isothermal cooling (0.5 and 0.05 °C/min) and heating (0.5 °C/min) experiments were carried out with the $Di_{90}An_{10}$ and $Di_{60}Fo_{30}An_{10}$ specimens of low melt fractions. The following results were obtained.

The dihedral angle in isothermal (equilibrium) experiments was lower at high temperatures and higher at low temperatures. This tendency corresponds to those reported in many metallic binary systems.

The dihedral angle under non-equilibrium conditions was different from the equilibrium value. During the cooling (crystal growth) process, the dihedral angle increased with the increasing cooling rate. In contrast, the dihedral angle decreased in the heating (dissolution or melting) system.

When the dihedral angle increased up to $\sim 60°$ in the cooling experiment, crystal clustering and melt segregation occurred. This resulted in expulsion of the melt from the crystal aggregate to reduce the total interfacial energy. The clusters collapsed into individual crystal grains when cooling was stopped and the dihedral angle returned to the equilibrium value. These observations provide powerful evidence that the change of interfacial energy ratio under non-equilibrium conditions is an actual process causing the textural change.

Natural clustering textures, such as the glomeroporphyritic texture in volcanic rocks and the clustering texture in granitic rocks, can be formed by melt expulsion depending on the increase of interfacial energy ratio (dihedral angle). We present a model producing textural variation depending on the interfacial energy ratio during cooling. The decrease in the interfacial energy ratio during heating is also important in partially molten geological systems such as in migmatite development.

Acknowledgements We would like to thank Y. Takei for her helpful advice and discussion on the interfacial energy and dihedral angle in partially molten systems. We would also like to thank S. Nakashima for his encouragement and for providing the computer software Ultimage. Useful discussions with H. Nagahara, H. Iwamori, S. Nakada, S. Sasaki, M. Kitamura, A. Tsuchiyama, T. Nakano, R. Morishita, M. Nakamura, K. Saiki, S. Suzuki, T. Hiraga, T. Terada, N. Geshi, and K. Mibe are gratefully acknowledged. Thanks are extended to H. Yamato for staining granite specimens. We would like to thank M. Takahashi for providing samples of the Sakura-jima volcanic rock and the Japanese Atomic Energy Research Institute for providing the Inada granite sample. We are also grateful to D. Walker and an anonymous reviewer for helpful and constructive comments which improved the manuscript. The measurements of dihedral angle on the digitized images were performed using the public domain NIH Image Program (developed at the US National Institute of Health). This research was supported in part by a research fellowships of the Japanese Society for the Promotion of Science for Young Scientists, and a grant-in-aid for scientific research from the Japanese Ministry of Education, Science, and Culture (to S. I.).

References

Askay IA, Hoge CE, Pask JA (1974) Phase distribution in solid-liquid-vapor systems. In: Frechette VD, Lacourse WC, Burdick VL (eds) Surfaces and interfaces of glass and ceramics. Plenum Press, New York, pp 299–321

Bard JP (1986) Microtextures of igneous and metamorphic rocks. Reidel, Dordrecht

Beere W (1975) A unifying theory of the stability of penetrating liquid phases and sintering pores. Acta Metall 23:131–138

Bryon DN, Atherton MP, Hunter RH (1994) The description of the primary textures of ''Cordilleran'' granitic rocks. Contrib Mineral Petrol 117:66–75

Bryon DN, Atherton MP, Hunter RH (1995) The interpretation of granitic textures from serial thin sectioning, image analysis and three-dimensional reconstruction. Mineral Mag 59:203–211

Bryon DN, Atherton MP, Cheadle MJ, Hunter RH (1996) Melt movement and the occlusion of porosity in crystallizing granitic systems. Mineral Mag 60:163–171

Bulau JR, Waff HS, Tyburczy JA (1979) Mechanical and thermodynamic constraints on fluid distribution in partial melts. J Geophys Res 84:6102–6108

Camel D, Eustathopoulos N, Desré P (1980) Chemical adsorption and temperature dependence of the solid-liquid interfacial tension of metallic binary alloys. Acta Metall 28:239–247

Cashman KV (1990) Textural constraints on the kinetics of crystallization of igneous rocks. In: Nicholls J, Russell JK (eds) Modern methods of igneous petrology: understanding magmatic processes. Reviews in mineralogy, vol 24. Mineral Soc Am, Washington, pp 259–314

Cooper RF, Kohlstedt DL (1986) Rheology and structure of olivine-basalt partial melts. J Geophys Res 91:9315–9323

Donaldson CH (1975) Calculated diffusion coefficients and the growth rate of olivine in a basalt magma. Lithos 8:163–174

Donaldson CH (1976) An experimental investigation of olivine morphology. Contrib Mineral Petrol 57:187–213

Donaldson CH (1979) An experimental investigation of the delay in nucleation of olivine in mafic magmas. Contrib Mineral Petrol 69:21–32

Donaldson CH, Williams RJ, Lofgren G (1975) A sample holding technique for study of crystal growth in silicate melts. Am Mineral 60:324–326

Eustathopoulos N, Coudurier L, Joud JC, Desré P (1974a) Étude thermodynamique de la tension interfaciale solide/liquide pore un systeme métallique binaire. III. Étude expérimentale du système Cu-Pb. J Chim Phys 71:1465–1471

Eustathopoulos N, Joud JC, Desré P (1974b) Étude thermodynamique de la tension interfaciale solide/liquide pore un

systeme métallique binaire. II. Applications. J Chim Phys 71:777–787
Eustathopoulos N, Coudurier L, Joud JC, Desré P (1976) Tension interfaciale solide-liquide des systèmes Al-Sn, Al-In et Al-Sn-In. J Crystal Growth 33:105–115
Faul UH (2000) Constraints on the melt distribution in anisotropic polycrystalline aggregates undergoing grain growth. In: Bagdassarov N, Laporte D, Thompson AB (eds) Physics and chemistry of partially molten rocks. Kluwer, Dordrecht, pp 67–92
Fenn PM (1977) The nucleation and growth of alkali feldspars from hydrous melts. Can Mineral 15:135–161
Fujii N, Osamura K, Takahashi E (1986) Effect of water saturation on the distribution of partial melt in the olivine-pyroxene-plagioclase system. J Geophys Res 91:9253–9259
Gaetani GA, Grove TL (1999) Wetting of mantle olivine by sulfide melt: implications for Re/Os ratios in mantle peridotite and late-stage core formation. Earth Planet Sci Lett 169:147–163
Grove TL, Walker D (1977) Cooling histories of Apollo 15 quartz-normative basalts. Proc Lunar Planet Sci Conf 8th, pp 1501–1520
Harte B, Hunter RH, Kinny PD (1993) Melt geometry, movement and crystallization, in relation to mantle dykes, veins and metasomatism. Philos Trans R Soc Lond A 342:1–21
Holness MB (1993) Temperature and pressure dependence of quartz-aqueous fluid dihedral angles: the control of adsorbed H_2O on the permeability of quartzites. Earth Planet Sci Lett 117:363–377
Holness MB (1995) The effect of feldspar on quartz-H_2O-CO_2 dihedral angles at 4 kbar, with consequences for the behavior of aqueous fluids in migmatite. Contrib Mineral Petrol 118:356–364
Houghton HF (1980) Refined techniques for staining plagioclase and alkali feldspars in the thin section. J Sediment Petrol 50:629–631
Hunter RH (1987) Textural equilibrium in layered igneous rocks. In: Parsons I (ed) Origins of igneous layering. Reidel, Dordrecht, pp 473–503
Ikeda S, Nakashima S (1999) Rolling experiment with partially molten rocks: a new apparatus and some experiments on the kinetics of material transport, dissolution and crystal growth. Eur J Mineral 11:441–453
Jerram DA, Cheadle MJ, Hunter RH, Elliott MT (1996) The spatial distribution of grains and crystals in rocks. Contrib Mineral Petrol 125:60–74
Jurewicz SR, Watson EB (1984) Distribution of partial melt in a felsic system: the importance of surface energy. Contrib Mineral Petrol 85:25–29
Jurewicz SR, Watson EB (1985) The distribution of partial melt in granitic system: the application of liquid phase sintering theory. Geochim Cosmochim Acta 49:1109–1121
Jurewicz SR, Jurewicz AJG (1986) Distribution of apparent angles on random sections with emphasis on dihedral angle measurements. J Geophys Res 91:9277–9282
Kirkpatrick RJ (1974) Kinetics of crystal growth in the system $CaMgSi_2O_6$-$CaAl_2SiO_6$. Am J Sci 274:215–242
Kirkpatrick RJ (1975) Crystal growth from the melt: a review. Am Mineral 60:798–814
Kirkpatrick RJ (1981) Kinetics of crystallization of igneous rocks. In: Lasaga AC, Kirkpatrick RJ (eds) Kinetics of geochemical processes. Reviews in mineralogy, vol 8. Mineral Soc Am, Washington, pp 321–398
Kirkpatrick RJ, Robinson GR, Hays JF (1976) Kinetics of crystal growth from silicate melts: anorthite and diopside. J Geophys Res 81:5715–5720
Kirkpatrick RJ, Klein L, Uhlmann DR, Hays JF (1979) Rates and processes of crystal growth in the system anorthite-albite. J Geophys Res 84:3671–3676
Laporte D (1994) Wetting behavior of partial melts during crustal anatexis: the distribution of hydrous silicic melts in polycrystalline aggregates of quartz. Contrib Mineral Petrol 116:486–499
Laporte D, Watson EB (1995) Experimental and theoretical constraints on the melt distribution in crustal sources: the effect of crystalline anisotropy on melt interconnectivity. Chem Geol 124:161–184
Laporte D, Rapaille C, Provost A (1997) Wetting angles, equilibrium melt geometry, and the permeability threshold of partially molten crustal protholiths. In: Bouchez JL, Hutton DHW, Stephens WE (eds) Granite: from segregation of melt to emplacement fabrics. Kluwer, Dordrecht, pp 31–54
Laporte D, Provost A (2000) The grain-scale distribution of silicate, carbonate and metallosulfide partial melts: a review of theory and experiments. In: Bagdassarov N, Laporte D, Thompson AB (eds) Physics and chemistry of partially molten rocks. Kluwer, Dordrecht, pp 93–140
Lasaga AC (1998) Kinetic theory in the earth sciences. Princeton University Press, Princeton
Lofgren G (1974) An experimental study of plagioclase crystal morphology: isothermal crystallization. Am J Sci 274:243–273
Lofgren G (1980) Experimental studies on the dynamic crystallization of silicate melts. In: Hargraves RB (ed) Physics of magmatic processes. Princeton University Press, Princeton, pp 487–551
Lofgren G (1983) Effect of heterogeneous nucleation on basaltic textures: a dynamic crystallization study. J Petrol 24:229–255
Lofgren G, Grove TL, Brown RW, Smith DP (1979) Comparison of dynamic crystallization techniques on Apollo 15 quartz normative basalts. Proc Lunar Planet Sci Conf 10th, pp 423–438
Lupulescu A, Watson EB (1999) Low melt fraction connectivity of granitic and tonalitic melts in a mafic crustal rock at 800 °C and 1 GPa. Contrib Mineral Petrol 134:202–216
Maaløe S, Wyllie PJ (1975) Water content of a granite magma deduced from the sequence of crystallization determined experimentally with water-undersaturated conditions. Contrib Mineral Petrol 52:175–191
Mibe K, Fujii T, Yasuda A (1998) Connectivity of aqueous fluid in the Earth's upper mantle. Geophys Res Lett 25:1233–1236
Mibe K, Fujii T, Yasuda A (1999) Control of the location of the volcanic front in island arcs by aqueous fluid connectivity in the mantle wedge. Nature 401:259–262
Morishita R, Obata M (1995) A new statistical description of the spatial distribution of minerals in rocks. J Geol 103:232–240
Muncill GE, Lasaga AC (1987) Crystal-growth kinetics of plagioclase in igneous systems: one-atmosphere experiments and application of simplified growth model. Am Mineral 72:299–311
Muncill GE, Lasaga AC (1988) Crystal-growth kinetics of plagioclase in igneous systems: isothermal H_2O-saturated experiments and extension of a growth model to complex silicate melts. Am Mineral 73:982–992
Nakano T, Fujii N (1989) The multiphase grain control percolation: its implication for a partially molten rock. J Geophys Res 94:15653–15661
Naney MT, Swanson SE (1980) The effect of Fe and Mg on crystallization in granitic systems. Am Mineral 65:639–653
Osborn EF (1942) The system $CaSiO_3$-diopside-anorthite. Am J Sci 240:751–788
Osborn EF, Tait DB (1952) The system diopside-forsterite-anorthite. Am J Sci, Bowen Vol:413–433
Park H-H, Yoon DN (1985) Effect of dihedral angle on the morphology of grains in a matrix phase. Metall Trans A, 16A:923–928
Passerone A, Eustathopoulos N, Desre P (1977) Interfacial tensions in Zn, Zn-Sn and Zn-Sn-Pb systems. J Less-Common Metals 52:37–49
Passerone A, Sangiorgi R, Eustathopoulos N, Desre P (1979) Microstructure and interfacial tensions in Zn-In and Zn-Bi alloys. Metal Sci June:359–365
Philpotts AR, Shi J, Brustman C (1998) Role of plagioclase crystal chains in the differentiation of partly crystallized basaltic magma. Nature 395:343–346
Philpotts AR, Brustman CM, Shi J, Carlson WD, Denison C (1999) Plagioclase-chain networks in slowly cooled basaltic magma. Am Mineral 84:1819–1829

Riegger OK, Vlack LHV (1960) Dihedral angle measurement. Trans Metall Soc AIME 218:933–935
Riley GN Jr, Kohlstedt DL (1991) Kinetics of melt migration in upper mantle-type rocks. Earth Planet Sci Lett 105:500–521
Smith CS (1948) Grains, phases, and interfaces: an interpretation of microstructure. AIME Trans 175:15–51
Swanson SE (1977) Relation of nucleation and crystal-growth rate to the development of granite textures. Am Mineral 62:966–978
Swanson SE, Fenn PM (1986) Quartz crystallization in igneous rocks. Am Mineral 71:331–342
Takei Y, Shimizu I (2001) Compositional dependence of dihedral angles in partially molten systems: thermostatistical models. Proc Deform Mech Rheol Tect, Noordwijkerhout, Netherlands, p 160
Toramaru A, Fujii N (1986) Connectivity of melt phase in a partially molten peridotite. J Geophys Res 91:9239–9252
Tsuchiyama A (1983) Crystallization kinetics in the system $CaMgSi_2O_6$-$CaAl_2Si_2O_8$: the delay in nucleation of diopside and anorthite. Am Mineral 68:687–698
Tsuchiyama A (1985) Crystallization kinetics in the system $CaMgSi_2O_6$-$CaAl_2Si_2O_8$: development of zoning and kinetics effects on element partitioning. Am Mineral 70:474–486
von Bargen N, Waff H (1986) Permeabilities, interfacial areas and curvatures of partially molten systems: results of numerical computations of equilibrium microstructures. J Geophys Res 91:9261–9276
von Bargen N, Waff H (1988) Wetting of enstatite by basaltic melt at 1350 °C and 1.0- to 2.5 GPa pressure. J Geophys Res 93:1153–1158
Waff HS, Bulau JR (1979) Equilibrium fluid distribution in an ultramafic partial melt under hydrostatic stress conditions. J Geophys Res 84:6109–6114
Waff HS, Faul UH (1992) Effects of crystalline anisotropy on fluid distribution in ultramafic partial melts. J Geophys Res 97:9003–9014
Wager LR, Brown GM, Wadsworth WJ (1960) Types of igneous cumulates. J Petrol 1:73–85
Walker D, Kirkpatrick RJ, Longhi J, Hays JF (1976) Crystallization history of lunar picritic basalt sample 12002: phase-equilibria and cooling-rate studies. Geol Soc Am Bull 87:646–656
Walker D, Powell MA, Lofgren GE, Hays JF (1978) Dynamic crystallization of an eucrite basalt. Proc Lunar Planet Sci Conf 9th, pp 1369–1391
Walker D, Jurewicz S, Watson EB (1988) Adcumulus dunite growth in a laboratory thermal gradient. Contrib Mineral Petrol 99:306–319
Watson EB (1982) Melt infiltration and magma evolution. Geology 10:236–240
Watson EB (1999) Lithologic partitioning of fluids and melts. Am Mineral 84:1693–1710
Watson EB, Brenan JM, Baker DR (1990) Distribution of fluids in the continental mantle. In: Menzies MA (ed) Continental mantle. Clarendon Press, Oxford, pp 115–125
Watson EB, Lupulescu A (1993) Aqueous fluid connectivity and chemical transport in clinopyroxene-rich rocks. Earth Planet Sci Lett 117:279–294
Williams H, Turner FJ, Gilbert CM (1954) Petrography : An introduction to the study of rocks in thin sections. WH Freeman, San Francisco